SAND98-2786J

Model Etch Profiles for Ion Energy Distribution Functions in an Inductively Coupled Plasma Reactor

Wenjing Chen and Barbara Abraham-Shrauner,
Department of Electrical Engineering, Washington University,
1 Brookings Drive, St. Louis, MO 63130

Joseph R. Woodworth,
Laser, Optics, and Remote Sensing Department, Sandia National Laboratories,
Albuquerque, New Mexico 87185-1423

Abstract

Rectangular trench profiles are modeled with analytic etch rates determined from measured ion distribution functions. The pattern transfer step for this plasma etch is for trilayer lithography. Argon and chlorine angular ion energy distribution functions measured by a spherical collector ring analyzer are fit to a sum of drifting Maxwellian velocity distribution functions with anisotropic temperatures. The fit of the model ion distribution functions by a simulated annealing optimization procedure converges adequately for only two drifting Maxwellians. The etch rates are proportional to analytic expressions for the ion energy flux. Numerical computation of the etch profiles by integration of the characteristic equations for profile points and connection of the profiles points is efficient.

DISCLAIMER

DISCLAIMER

Portions of this document may be illegible in electronic image products. Images are produced from the best available original document.

I. Introduction

Plasma etching is an important step in integrated circuit fabrication. Glow discharge processes and complex chemical and physical interactions involved in the etching plasma have been extensively studied but are still not well understood, so that at present plasma etching processes are designed and optimized empirically. The empirical approach is expensive and time consuming since there are many independent parameters involved in a plasma etching process. Increased wafer size and process steps and decreased feature size make empirical approaches more complicated and more expensive. It is desirable to understand and evaluate the evolution of etch profiles by a theoretical approach. Modeling and simulation furnish better understanding of the etch process and give guidance to the experiments.

The increasing device density has accelerated the need for both preservation of wafer surface area and device isolation. Trench etching is one method that has been used for the fabrication of trench capacitor and device isolation. Trench etching is a complex application of plasma etching. The etching process produces deep, high aspect ratio trenches. Etch depths may reach 10 μm or more with aspect ratios of 10:1 or greater. Typical dimensions are 0.35 to 1.0 μm in width and 2 to 5 μm in depth.[1] Trench etching requires near-vertical, slightly inwardly sloped sidewalls with no undercut and smooth, rounded bottoms. Although sloped walls are highly desirable to eliminate the formation of a void in the trench during the deposition process used to refill the trench,[2] near-vertical sidewalls are needed for minimizing the device area. Smooth, rounded bottoms minimize the effect of thermal stresses on the silicon crystal during the deposition process and also minimize the effects of mechanical stresses on the film. Excess stress

will ultimately result in defects in the oxide. It is desired to control the trench etch profiles precisely.

To simulate the etch profiles we need to understand the processes that control the etch rate. A simple etch model based on Langmuir adsorption kinetics[3,4] suggests that the total etch rate with both ions and neutrals is greater than the etch rates with either species alone. In the ion flux-limited regime the etch rate is proportional to the ion energy flux. This result has been verified experimentally for several planar systems[5,6]. The calculation of ion energy flux requires an ion distribution function.

Kawamura et al.[7] present a review of previous works on ion energy distribution functions arriving at the target in the collisionless regime of a capacitively coupled RF discharge. Most calculations of the ion energy distribution function (IEDF) rely on numerical methods. The calculation methods of the IEDF can be classified as an approximate analytical model, a numerical integration of the equations of motion, a Monte Carlo simulation, a Monte Carlo-fluid hybrid model, a particle-in-cell method and a particle-in-cell combined with Monte Carlo collisions.

The ion energy distribution function is frequently simulated by a Monte Carlo simulation. The Monte Carlo simulation follows the transport paths of many ions through the sheath. Although the spatial field variation across the sheath is dependent on the collision mechanism, this is presently not calculated self-consistantly for most simulations. This allows each ion trajectory to be calculated independently from others.[8] Generally the Monte Carlo simulation follows the trajectory of each ion through the sheath, determines its bombardment properties and

sums the results for many ions.[9] The advantages of the Monte Carlo simulation are the detailed results and the simulation is more realistic if the process parameters are known. The input parameters usually are the electric field profile in the sheath, the collision cross section, the ratio of sheath thickness to mean free path and the frequency. The disadvantage is that the input parameters are not always known from experimental measurements.

The computer program SPEEDIE calculates the angular and energy distribution of ions and fast neutrals by using a Monte Carlo simulator for the ion sheath transport.[8] It gives the ion distribution function with respect to energy and angle, and the ion angular distribution function. Liu et al. [10] used a Monte Carlo simulation to simulate the ion angular energy distribution functions at different pressures. There are some disagreements between their Monte Carlo simulation and their experimental data especially at 10 mTorr pressure. Hoekstra et al.[11] produced the energy and angular distributions of ions and neutrals by a Monte Carlo simulation. They calculate the trajectories of ions and neutrals by using the sources of the plasma species, the time dependent electric fields, and the time dependent sheath properties generated by their hybid plasma equipment mode. Manenschijn and Goedheer[12] calculated the angular ion and neutral energy distribution functions using a Monte Carlo method that includes charge exchange and elastic scattering.

Gottscho[13] discussed several ion velocity distribution functions for the new generation of low pressure, high density plasma reactors where velocities are parallel and perpendicular to the magnetic field. Case one is a two-temperature distribution function, where the velocity distribution function is the product of Maxwellians for the parallel and perpendicular velocities

with different temperatures. This case is for a situation where the sheath voltage is neglected. In case two the velocity distribution function is a product of a Maxwellian for the perpendicular velocities and a delta function for the parallel velocities. Case two is for a situation where ions with finite perpendicular temperature are accelerated across a collisionless sheath and gain the full sheath voltage. In case three the velocity distribution function is a product of a Maxwellian for the perpendicular velocities and a drifting Maxwellian for the parallel velocities. Case three includes a velocity spread in the velocity distribution function for the parallel velocities, which differs little from the case two for realistic plasma parameters. In case four the velocity distribution function is a product of a drifting Maxwellian for the perpendicular velocities and a delta function for the parallel velocities as in case two. Case four is for off-axis ion transport in strongly diverging magnetic fields. The assumptions for perpendicular velocity distribution functions are justified by experiments.[14-16]

Tokonami and Makabe[17] suggested a numerical model for an ion velocity distribution function based on the Boltzmann equation. The spatially local profiles of two-dimensional ion velocity distributions were calculated. The collision cross sections, sheath voltage and width, ion current density and pressure were used in their calculation. However the ion velocity distribution function is not two dimensional for the trench whose etch profile they were modeling.

Abraham-Shrauner and Wang suggested that the ion velocity distribution function in a collisionless sheath is a drifting Maxwellian function.[18] This model starts with a Maxwellian distribution for ions in the bulk plasma. When ions enter the sheath, the sheath field will accelerate the ions toward the wafer. If there are no collisions in the sheath, the ion distribution may be a drifting Maxwellian for some conditions. This assumption is consistent with the ion

distribution function measurement at low pressure where collisions can be neglected.[19] Chen and Abraham-Shrauner suggested that the sum of drifting Maxwellian functions is a possible ion velocity distribution function for a collisional sheath.[20]

In experiments a modified ion energy distribution function is defined, which is related to the ion velocity distribution function. The modified ion energy distribution function is frequently measured by a gridded retarding field energy analyzer. The modified ion energy distribution function is the derivative of the current collected by the analyzer with respect to the retarding potential. The modified ion energy distribution function is not normalized to the ion density if one integrates it over energy and angle; it must be multiplied by a normalization constant. A parallel retarding field energy analyzer measures the ion energy distribution function only in a direction parallel to the sheath field. A spherical retarding field energy analyzer measures the ion energy distribution function at different angles.

Modified ion energy distribution functions have been measured by many authors using parallel or spherical retarding field energy analyzers. Here we only mention some among them. Okamoto and Tamagawa[19] measured ion energy distribution functions at very low pressure in an RF plasma. Ingram and Braithwaite[21] measured the ion energy distributions at different pressures in a direction normal to their collector in a capacitively coupled RF argon discharge. Charles et al. [22,23] measured the ion energy distribution functions in a low pressure argon plasma diffusing from a 13.56 MHz helicon source. Junck and Getty[24] measured ion energy distribution functions for three magnetic field configurations in an electron cyclotron resonance Ar plasma. Kim and Chang[25] measured the ion energy distribution functions at different magnetic field strengths in

the helicon Ar plasma along the axial direction. Liu et al. [10] measured the angular ion energy distribution functions at several pressures in an RF Ar plasma. Woodworth et al. [26-28] measured the angular ion energy distribution functions in an inductively coupled reactor in chlorine, argon or chlorine-argon plasma.

We have reviewed modeling and simulation done by other researchers. This research furnished the theoretical and experimental basis for our work. Many researchers have modeled and simulated ion energy distribution function and etch profiles, but no one has related the etch profiles to the actual measured ion distribution functions in plasma reactors. The ion energy or angular distribution functions used in their etch profile simulations are either analytical or simulated by Monte Carlo simulation. Also, except for the earlier papers of our group[18,29] and an isotropic etch,[30] no one has used approximate analytic expressions for the etch rate. The purpose of our work is to fit the measured ion energy distribution functions using our model and then predict the etch profiles.

This paper models the etch profiles for a long trench for ion energy distribution functions in an inductively coupled plasma (ICP) reactor. The pattern transfer step is for trilayer lithography where the photoresist etches down to a silicon dioxide mask and the trench is etched in the substrate. We assume that the yield per ion in etching is approximately proportional to its energy and independent of its angle relative to the surface normal. Then the etch rate is proportional to the ion energy flux. We model the ion velocity and energy distribution function on the wafer surface and fit the energy distribution to the measured data using the simulated

annealing procedure. The ion energy flux is calculated from the ion velocity distribution function where the etch rate is proportional to the ion energy flux in ion energy flux-limited etching.

The topics are organized as follows. The ion velocity and energy distribution functions for an ICP reactor are discussed in Sec. II. The fitting of ion energy distribution to the measured data is given in the Sec. III. The calculation of etch profiles is presented in Sec. IV. The conclusions are given in Sec. V.

II. Ion Velocity and Energy Distribution Functions for an ICP Reactor

The plasma in an ICP reactor is generated by the application of RF power to a nonresonant inductive coil. The coil configuration is either cylindrical or planar. The coils are commonly driven by RF power. The plasma forms when the gas near the coil is ionized by the induced RF electrical field. Power is transferred from the electrical fields to the plasma electrons by collisional dissipation. At low pressure (< 10 mtorr), this power transfer may also furnished by a collisionless heating process, in which bulk plasma electrons are accelerated and thermalized by the oscillating inductive fields.[31] The power is transfered within a thin layer near the plasma surface.

The ICP reactor used by Woodworth et. al.[26,27] is a "GEC Reference Cell" that has been modified to produce an inductively coupled plasma. The original GEC Reference Cell is a parallel plate, capacitively-coupled, RF plasma reactor. The modified inductively coupled GEC cell replaces the standard parallel-plate upper-electrode assembly with a five-turn planar coil coupled to the plasma through a silica window. The lower electrode is grounded. The gas is fed into chamber through one of the side ports of the GEC cell and is pumped out through the

plenum at the bottom of the cell and the gate valve on the side of the cell. The feed gas is argon or chlorine. A gridded energy analyzer is placed behind a pinhole in the lower electrode in a separate vacuum system. The pinhole has a diameter of 3-10 μm that varies in different experiments. The ion energy analyzer consisted of three spherical grids and electrically isolated annular rings that were on a hemispherical surface. The radius of the hemispherical surface is 2.29 cm. The rings had an angular width in θ of approximately 4°. The first and third grids have 92% transparency each and the second grid has a transparency of 81%. The transparency is the percentage of the open area that allows ions to be transmitted. The first grid is grounded to created a field free region between pinhole and the detector. The second grid is biased form 0 to 40 V to allow those ions with energy greater than its potential energy to pass through to the collecting plate. The third grid is biased negatively to block electrons and prevent secondary electron emission. With this configuration, the analyzer can measure the ion energy distribution function with angular information.

We derive the expression for the modified ion energy distribution function as measured by spherical collector rings. Our expression differs from the total IEDF as it depends on the ion energy and the angle θ between the ion velocity vector and the electric field. The total IEDF is integrated over the angle θ. The data for these angular dependent IEDFs are of special interest since they contain information about the angular dependence of the ion distribution function. The angular dependence is necessary for the computation of the lateral etch rate in trenches.

The measured modified ion energy distribution function was found from the current measurements by taking the derivative of the current with respect to the ion retarding potential.

The current, I, collected by each annular electrode is related to the ion velocity distribution function at the pinhole position by

$$I = G\int_S \mathbf{J}\cdot d\mathbf{S}, \tag{1}$$

where $\mathbf{J} = q\int \mathbf{v}f(\mathbf{v})d^3v$, G is the total transparency of the analyzer grids, S is the area of the pinhole, q is the ion charge, $\mathbf{v}$ is the ion particle velocity and d^3v is the three-dimensional volume element in velocity space.

Since the radius of the collecting sphere is much larger than the pinhole diameter, we can view the pinhole as a point and all ions come along the radial direction through the center of the pinhole. Then Eq. (1) can be approximated as

$$I \approx Gq\int_S\int f(\mathbf{v})vd^3v\cos\theta\, dS \approx GqS\int_{v_{\min}}^{v_{\max}} vf(\mathbf{v})v^2dv\int_{\theta_1}^{\theta_2} \sin\theta\cos\theta d\theta\int_0^{2\pi} d\varphi, \tag{2}$$

where $v_{\min}$ is related to the ion retarding potential V by equation $\frac{1}{2}mv_{\min}^2 = qV$. The velocity integral is over spherical velocity coordinates where θ is the angle between the normal to the pinhole area and the ion velocity vector. Eq. (2) is valid for distances large compared to the pinhole diameter.[27]

The ion velocity distribution function $f(\mathbf{v})$ is chosen as a sum of drifting Maxwellian functions with anisotropic temperatures[13,32] given by

$$f = \sum_{l=1}^{L} n_l \left(\frac{m}{2\pi k_B T_{\perp l}}\right)\left(\frac{m}{2\pi k_B T_{\| l}}\right)^{1/2} \exp\left[-\frac{m v_\perp^2}{2 k_B T_{\perp l}}\right] \exp\left[-\frac{m}{2 k_B T_{\|}}(v_{\| l} - u_l)^2\right] \quad (3)$$

where $T_{\perp l}$ and $T_{\| l}$ are the ion temperatures perpendicular and parallel to the direction of the magnetic field of the reactor for the lth term in the expansion, $v_\perp$ and $v_\|$ are the individual ion velocities perpendicular and parallel to the axis of the reactor, u_l is the magnitude of the ion drift velocity $\mathbf{u}_l$ which is along the z axis for the lth term in the expansion, k_B is the Boltzmann constant, and m is the ion mass.

We chose the ion velocity distribution function $f(\mathbf{v})$ as a sum of drifting Maxwellian functions with anisotropic temperatures rather than the model with isotropic temperatures as suggested in earlier work,[20] since the model with isotropic temperatures could not fit the experimental data.

The modified ion energy distribution function is the derivative of the current I from Eqs. (2) and (3) with respect to the ion retarding potential V given by

$$-\frac{d(I/A_\theta)}{dV} \approx \sum_{l=1}^{L} N_{sl} \beta_{\| l}^{1/2} \beta_{\perp l} E \cos\theta_m \cdot$$

$$Exp[-\beta_{\| l}(E\cos^2\theta_m - 2\sqrt{EE_l'}\cos\theta_m + E_l' + \alpha_l E \sin^2\theta_m)] \quad (4)$$

where $E = \frac{1}{2}mv^2$ is the ion particle energy,

$$N_{sl} = \frac{Gq^2 n_l S}{2^{1/2} m^{1/2} r^2 \pi^{3/2}},\ \beta_{\|l} = \frac{1}{k_B T_{\|l}},\ \beta_{\perp l} = \frac{1}{k_B T_{\perp l}},\ E_l' = \frac{1}{2}mu_l^2,$$
$$A_\theta = 2\pi r^2(\cos\theta_1 - \cos\theta_2), \theta_m = \frac{\theta_1 + \theta_2}{2}, \alpha_l = \frac{T_{\|l}}{T_{\perp l}}. \quad (5)$$

Here θ_1 and θ_2 are the angular positions of the ring edges measured from the normal of the pinhole area and A_θ is the area of the collector ring. The modified ion energy distribution function in Eq. (4) has been corrected for the different areas of the collector rings. The detailed derivation is given in Appendix A.

III. Model IEDFs in an ICP Reactor

Using the optimum parameter sets found by the simulated annealing procedure[20] we fit the IEDF data from the ICP reactor by the modified IEDF model in Eq. (4). First we tried the sum of drifting Maxwellians with isotropic temperatures and found that we could not fit the measured data well. Then we tried the sum of drifting Maxwellians with anisotropic temperatures. The modified IEDFs have a very narrow energy interval and single peak. From the simulation, we found that the cost function decreases as the number of terms increases and two terms of anisotropic drifting Maxwellians fit the data well. More than two terms of drifting Maxwellian improved the fit to the tiny peaks of the ion energy distribution function but did not improve the fit to the dominant peaks much. We chose two anisotropic drifting Maxwellian distributions to fit the data.

The parameters found from simulated annealing are given in Table 1. The dominant term is #1 for Ar and #2 for Cl_2. For each gas each column constitutes a set of $(N_s, E', T_{\parallel}, T_{\perp})$ for an anisotropic drifting Maxwellian in the sum. The simulated annealing was carried out with $\beta_{\parallel}$ and $\beta_{\perp}$ but the corresponding temperatures are listed in Table 1. The expressions for these parameters have been given in Eq. (5).

Fig. 1 shows the plots of the simulated and measured IEDFs from an ICP reactor with an argon plasma. The curves of a, b, c and d correspond to the measurements of electrode with mean angles of 1.56°, 5.81°, 10.59° and 15.03° respectively. Fig. 2 shows the plots of the simulated and measured IEDFs from ICP reactor with a chlorine plasma. The curves of a, b, c and d correspond to the measurements of electrode with mean angles of 1.56°, 5.67°, 10.3° and 14.4° respectively. The dots are the measured data. The peak position of the IEDF in the argon plasma is located at a higher energy than that in the chlorine plasma. Both IEDFs have a narrow energy spread and the IEDFs in the chlorine plasma have a narrower energy spread than those in the argon plasma. In the ICP reactor the sheaths are collisionless under most operating conditions. Typical sheath thicknesses in the ICP reactor are less than 1 mm while typical mean free paths for elastic and charge transfer collisions between ions and neutrals are ten times larger.[13] The ions may experience some collisions in the presheath but these do not produce the low energy tail found in the MIT data for argon[10] where the mean free path was equal to or smaller than the sheath thickness. The peaks of the ion IEDFs do fall off less rapidly for ions incident at angles off the normal direction to the electrodes than the argon IEDFs did in the MIT measurements. This slower fall off of the IEDFs with increasing angle indicates a perpendicular temperature greater than the parallel temperature of the IEDF as the thermal spread is much

broader in the perpendicular direction. The exponential decay factor at the peak of the IEDF as a function of the angle can computed for a single two-temperature drifting Maxwellian. The simulation results show that sum of drifting Maxwellians with anisotropic temperature is a possible ion velocity distribution function for an ICP reactor.

IV. Etch Profiles

The etched surface of a long trench is illustrated in Fig. 3. Ideally the trench has vertical sidewalls and a rounded bottom. D_{pr} is the thickness of the photoresist, D_m is the thickness of the silicon dioxide mask, D_S is the thickness of the semiconductor, and w is the width of the trench opening. The surface is exposed to reactive neutrals and energized ions. The neutrals come in all the directions. The ions come mostly in the direction perpendicular to the surface. The etched surface is described by an evolution equation.[29, 33]

$$\frac{\partial F}{\partial t} + \mathbf{v_e} \cdot \nabla \mathbf{F} = 0 \tag{6}$$

for F the equation of the etch profile. The etch rate ER is the normal component of the velocity $\mathbf{v_e}$ of the moving surface.

We assume that the velocity of the etched surface is proportional to the ion energy flux. For the etching of a long trench, from Eq. (6) we obtain

$$\frac{d\bar{y}}{d\bar{t}} = \bar{\mathcal{E}}_y, \qquad \frac{d\bar{z}}{d\bar{t}} = \bar{\mathcal{E}}_z, \tag{7}$$

where the dimensionless variables are $\bar{z} = 2\frac{z}{w}$, $\bar{y} = 2\frac{y}{w}$, $\bar{t} = \frac{tkmnu^3}{w}$, (8)

$$\bar{\mathcal{E}}_y = \frac{2\mathcal{E}_y}{mnu^3}, \quad \bar{\mathcal{E}}_z = \frac{2\mathcal{E}_z}{mnu^3}, \tag{9}$$

w is the trench width and k is the proportionality constant between the etch rate and the ion energy flux. The total ion density n and ion drift velocity magnitude u are

$$n = \sum_{l=0}^{L} n_l, \quad u = \frac{1}{n}\sum_{l=1}^{L} n_l u_l. \tag{10}$$

The product $kmnu^3/2$ is roughly the etch rate in the midplane (y = 0) of the trench such that the characteristic time is roughly one-half the trench width divided by the etch rate at the mid-plane of the trench.[18] The advantage of putting the equations in dimensionless form is that we can see clearly how many independent parameters there are. Also we eliminate the need for k values since there are little experimental data for k and their values vary for different systems.

We assume the etch rate is proportional to the ion energy flux in the ion-flux limit regime. The ion energy flux $\mathcal{E}$ for a trench can be defined in terms of the ion velocity distribution function f. The vector components of the ion energy flux can be expressed as integrals over cylindrical velocity coordinates. They are

$$\varepsilon_y = \frac{m}{2}\int_0^\infty \int_0^\infty \int (v_\perp^2 + v_{||}^2) v_\perp^2 \cos\varphi f dv_\perp dv_{||} d\varphi ,$$

$$\varepsilon_z = \frac{m}{2}\int_0^\infty \int_0^\infty \int (v_\perp^2 + v_{||}^2) v_\perp v_{||} f dv_\perp dv_{||} d\varphi , \tag{11}$$

where f is given by Eq (3). The integral limits for the azimuthal angle are ϕ_a to π-ϕ_a and π+ϕ_b to 2π-ϕ_a. The expressions for ϕ_a and ϕ_b can be found in references.[18,20,33] The bounds on ϕ are determined by the feature geometry, which accounts for ion shadowing by the photoresist and etch mask.

The approximate expressions for the components of the energy flux have been calculated for a drifting Maxwellian with anisotropic temperatures.[34] Again the general ion velocity distribution function is a sum of anisotropic drifting Maxwellian functions f_l. The energy flux components of the energy flux for the f_l are:

$$\varepsilon_{yl} \approx \frac{m n_l u_l^3}{4\sqrt{\pi} U_l \alpha_l^{1/2}} \left\{ \frac{(1+b^2)\exp\left[-\frac{U_l^2 b^2 \alpha_l}{(1+b^2\alpha_l)}\right]}{(1+b^2\alpha_l)^{5/2}} - \frac{(1+a^2)\exp\left[-\frac{U_l^2 a^2 \alpha_l}{(1+a^2\alpha_l)}\right]}{(1+a^2\alpha_l)^{5/2}} \right\}$$

$$\mathcal{E}_{zl} \approx \frac{mn_l u_l^3}{2}\left\{\frac{1}{2}+Sign(1-\bar{y})[\frac{1}{2}-\frac{(1+b^2)\exp[-\frac{U_l^2 b^2\alpha_l}{(1+b^2\alpha_l)}}{2(1+b^2\alpha_l)^{7/2}}+\frac{b\sqrt{\alpha_l}U_l}{\sqrt{\pi}}erfc(b\sqrt{\alpha_l}U_l)]\right.$$

$$\left.-\frac{(1+a^2)\exp[-\frac{U_l^2 a^2\alpha_l}{(1+a^2\alpha_l)}}{2(1+a^2\alpha_l)^{7/2}}+\frac{a\sqrt{\alpha_l}U_l}{\sqrt{\pi}}erfc(a\sqrt{\alpha_l}U_l)\right\}, \tag{12}$$

$$\text{where } a=\frac{1+\bar{y}}{\bar{z}+d(\bar{t})}, b=\frac{(1-\bar{y})Sgn(1-\bar{y})}{\bar{z}+0.5d(\bar{t})[Sgn(1-\bar{y})+1]}, \; d(\bar{t})=d_0+0.5[Sgn(t_0-\bar{t})+1](t_0-\bar{t}) \tag{13}$$

$$U_l=\frac{u_l}{v_{th}}, \; v_{th}=\sqrt{\frac{2KT_{\|l}}{m}}, \; \alpha_l=\frac{T_{\|l}}{T_{\perp l}}. \tag{14}$$

The function $d(\bar{t})$ models the etching of a photoresist down to an etching mask (usually oxide) which does not etch. The approximate expressions in Eqs. (12) are valid for $U_l >>1$.

When the ion velocity distribution function is a sum of anisotropic drifting Maxwellians, the approximate expressions for the energy flux at the wafer surface are:

$$\mathcal{E}_y \approx \sum_{l=1}^{L} \mathcal{E}_{yl}$$

$$\mathcal{E}_z \approx \sum_{l=1}^{L} \mathcal{E}_{zl}. \tag{15}$$

We assume that an etching plasma has the IEDFs we simulated and consider a long trench. The initial conditions for the surface trajectories are changed from $\bar{z} = 0$ at $\bar{t} = 0$ to $\bar{z} = 0.05 + 0.2\,(1 - 00.9375\,\bar{y})^{1/2}$ at $\bar{t} = 0$ for the initial values of $\bar{y}$ between 0 and 1.003 to avoid the singular behavior.[17] By symmetry we only consider positive $\bar{y}$. The two parameters determining the mask thickness and the initial photoresist thickness are fixed at $d_0 = 0.32$ and $t_0 = 1.867$.[17] If we change their values, the etch profiles will change since the acceptance angle for incident ions on the trench varies with the height of the photoresist and etching mask. Numerically integrating the characteristic equations (7) by Matlab, which is much faster than by Mathematica, we determine the points $(\bar{y}, \bar{z})$ on the etch profile at a given time $\bar{t}$. Once the points are calculated, the plots for the etch profiles are made by ListPlot on Mathematica.

The etch profiles in Fig. 4 for the ICP reactor with the argon plasma and Fig. 5 for the ICP reactor with the chlorine plasma correspond to the IEDF curves in Fig. 1 and Fig. 2. The trench opening is between y = -1 and y =1. The photoresist mask is not pictured. The aspect ratio is the ratio of etching depth to the width of the opening. When the aspect ratio is small, the curves in Figs. 1 and 2 are very similar. When the aspect ratio increases, the argon plasma profiles have less lateral etch and a more rounded bottom and the chlorine plasma profiles have more lateral etch and a flatter bottom.

From the etch profiles in Figs. 4 and 5 we find the etch rate will decrease as time increases. This is because the cut-off angles ϕ_a and ϕ_b are functions of the trench aspect ratio. As the aspect ratio increases, fewer particles will arrive at the etched surface, so that the etch rate will decrease.

In the above etch profile simulations we assume that the etching mask does not etch, but the photoresist etches which is modeled by the function d(t) given by Eq. (13). To see the effect of the height of photoresist on the etch profiles, we assume that both of the etching mask and photoresist do not etch. The Eq. (13) becomes

$$d(\bar{t}) = d_0 + t_0. \tag{16}$$

We plot the etch profiles for the ICP with the chlorine plasma in Fig. 6 using same IEDF parameters as in Fig. 2. We compare Fig. 5 and Fig. 6 and find that if the photoresist does not etch, the etch is a little slower than that if the photoresist etches. This is because that ϕ_a and ϕ_b are functions of $d(\bar{t})$. When the photoresist does not etch more bombarding particles will be blocked by the photoresist. The etch profiles in Figs 4-6 show more lateral etch and rounded bottom than usually seen in commercial etch profiles. The inclusion of passivation would alter these profiles to show straighter sidewalls. That has not been included here.

In the etch profile calculations above we used a dimentionless form. From Eq. (5) we see that if we know the parameters k, w, m, n, u, we can calculate the actual etch time t, vertical etch depth z and lateral etch width y. The parameters n and u from Eq. (10) can be calculated from the parameters n_l and u_l in N_{sl} and $E_l^{'}$ in Eq. (5) from the IEDF simulation. If we know the etching gas, we may know the ion mass m. In the argon plasma case, the ion is Ar^+ with mass 6.68×10^{-26} kg. In the chlorine plasma case, both Cl^+ and Cl_2^+ contribute to the IEDF. There is research evidence that the dominant ion is Cl^+[11,28]. So, in our calculation we use Cl^+ with mass 5.9285×10^{-26} kg. The constant k, the slope of the etch rate versus energy flux relationship, can be

obtained by experiment. There are few experimental data for the constant k. The only k we know is from Ding's paper for CF_4 etching of SiO_2,[6] which is 1.43×10^{-11} m^3/J and we use that. The radius of electrode r is 2.29 cm. The radius of pinhole is 2.5 μm for the argon plasma and 3 μm for the chlorine plasma. The total transparency G is 0.686. The charge q is 1.6×10^{-19} C. Assuming the trench width w is 1 μm, we calculate the etch time t corresponding to the dimensionless time $\bar{t} = 1$. Table 2 gives the actual parameters with dimensions that can be derived from the parameters obtained from the ICP reactor with the argon plasma simulation. Table 3 gives the actual parameters with dimensions that can be derived from the parameters obtained from the ICP with the chlorine plasma simulation.

From the calculation we found that the lateral etch rate has same order for the argon plasma and the chlorine plasma and the vertical etch rate for argon plasma is three times faster than that in chlorine plasma. There will be less undercut for the argon plasma than for the chlorine plasma if we etch same vertical depth. The perpendicular temperature in the chlorine plasma is higher than that in the argon plasma. It will contribute to the more undercut, since the chlorine plasma has more lateral thermal movement.

To verify the precision of parameters calculated above, we calculate the ion density from the measurements of ion current density. The ion current density in the ICP reactor with the argon plasma is 16.8 mA/cm^2 at 10mTorr and 200W.[26] We can calculate the ion current density by

$$J = q\int v_{\|} f(\mathbf{v}) d^3 v$$

$$= qn(\frac{m}{2\pi KT_{\|}})^{\frac{1}{2}}(\frac{m}{2\pi KT_{\perp}})\int_0^{2\pi} d\phi \int_0^{\infty} \exp(-\frac{m}{2KT_{\perp}} v_{\perp}^2) v_{\perp} dv_{\perp} \int_0^{\infty} v_{\|} \exp[-\frac{m}{2KT_{\perp}}(v_{\|} - u)^2] dv_{\|}$$

$$= qn\{\sqrt{\frac{KT_{\|}}{2\pi m}} \exp(-\frac{m}{2KT_{\|}} u^2) + \frac{u}{2}[1 + erf(u\sqrt{\frac{m}{2KT_{\|}}})]\}. \quad (17)$$

We obtain that the ion density is 1.09×10^{17} which is a little higher that 7.698×10^{16} given in table 2. The ion current density in the ICP reactor with the chlorine plasma is 6.7 mA/cm^2 at 30mTorr and 200W.[27] The calculation in Eq. (17) gives the ion density 5.76×10^{16} which is close to 7.23×10^{16} given in table 3.

V. Conclusions

The ion velocity distribution function in an ICP reactor is approximated by the sum of drifting Maxwellian distribution functions with anisotropic temperatures. The expression of the ion energy distribution function for spherical collector rings is derived using this velocity distribution function. A simulated annealing optimization technique is used to find the optimized parameters set to fit the measured IEDFs with angular dependence in an ICP reactor with the argon plasma and chlorine plasma. The calculated IEDFs fit the measured IEDFs well.

The etch profiles of a long trench are modeled for the measured IEDF data. The pattern transfer step is for trilayer lithography where the photoresist etches down to a silicon dioxide mask and the trench is etched in the substrate. The etch rate in the ion flux-limited regime varies as the ion energy flux which is calculated as an analytic expression from the ion velocity

distribution function. The etch profiles are computed numerically by integration of characteristic equations for the profile points and by numerical computation of the profile at a given time. Actual parameters and etch rate are calculated from the model parameters for the argon and chlorine plasma.

Acknowledgment: The research was supported by the National Science Foundation Grant ECS-9310408 and by the United States Department of Energy under contract DE-AC04-94AL85000. Sandia is a multiprogram laboratory operated by The Sandia Corporation, a Lockheed Martin Company, for the US. Department of Energy. We thank M. E. Riley at Sandia National Laboratories for discussions.

Appendix A

The ion velocity distribution function $f(\mathbf{v})$ is a drifting Maxwellian function with anisotropic temperatures given by

$$f = n\left(\frac{m}{2\pi KT_{\perp}}\right)\left(\frac{m}{2\pi KT_{\parallel}}\right)^{1/2} \exp\left[-\frac{mv_{\perp}^2}{2\,KT_{\perp}}\right]\exp\left[-\frac{m}{2\,KT_{\parallel}}(v_{\parallel}-u)^2\right]. \quad \text{(A-1)}$$

"$\parallel$" and "$\perp$" denote directions parallel to the z axis and perpendicular to it.

We rewrite $f(\mathbf{v})$ in cylindrical coordinates:

$$f = n\left(\frac{m}{2\pi\, kT_{\perp}}\right)\left(\frac{m}{2\pi\, kT_{\parallel}}\right)^{1/2} \exp\left[-\frac{m}{2kT_{\parallel}}(v\cos^2\theta - 2uv\cos\theta + u^2 + \alpha v^2\sin^2\theta)\right]. \quad \text{(A-2)}$$

We substitute Eq. (A-2) into Eq. (2) and approximate $\cos\theta$ in the exponential by $\cos\theta_m$, $\theta_m = (\theta_1+\theta_2)/2$, where $\theta_2 - \theta_1 \approx 4^\circ$. The validity of this approximation can be checked by doing the integral exactly over θ and expanding in small $\theta_2 - \theta_1$. We obtain the expression for the current I

$$\mathrm{I} \approx N_s A_\theta \beta_{\parallel}^{1/2}\beta_{\perp}\cos\theta_m \int_{qV}^{qV_{\max}} E\exp[-\beta_{\parallel}(E\cos^2\theta_m - 2\sqrt{EE'}\cos\theta_m + E' + \alpha E\sin^2\theta_m)]dE \quad \text{(A-3)}$$

The potential derivative of the current I is

$$-\frac{dI}{dV} = N_s A_\theta \beta_{\parallel}^{1/2} \beta_{\perp} E \cos\theta_m \exp[-\beta_{\parallel}(E\cos^2\theta_m - 2\sqrt{EE'}\cos\theta_m + E' + \alpha E \sin^2\theta_m)]. \quad \text{(A-4)}$$

After corrections for the different areas of the annular electrodes by dividing Eq. (A-4) by area A_θ, we obtain

$$-\frac{d(I/A_\theta)}{dV} = N_s \beta_{\parallel}^{1/2} \beta_{\perp} E \cos\theta_m Exp[-\beta_{\parallel}(E\cos^2\theta_m - 2\sqrt{EE'}\cos\theta_m + E' + \alpha E \sin^2\theta_m)]. \quad \text{(A-5)}$$

References

1. S. A. Campbell, *The Science and Engineering of Microelectronic Fabrication.* (Oxford University Press, New York, 1996).

2. S. M. Sze, *VLSI Technology.* (McGraw-Hill, New York, 1988).

3. T. M. Mayer and R. A. Barker, J. Electrochem. Soc. **129**, 585 (1982).

4. Michael A. Lieberman and Richard A. Gottscho, Physics of Thin Films. **18**, 1 (1994).

5. R. J. Visser and C. A. M. dc Vries, *Proceedings of the 8th International Symposium on Plasma Chemistry.* Edited by K. Akashi and A. Kinbara, IUPAC, Tokyo, 1029 (1987).

6. J. Ding, J.-S. Jeng, G.-H. Kim, H. L. Mayard, J. S. Hamers, N. Hershkowitz, and J. W. Taylor, J. Vac. Sci. Technol. A **11**, 1283 (1993).

7. E. Kawamura, V. Vahedi, M. A. Lieberman and C. K. Birdsall, Memorandum No. UCB/ERL M95/49, University of California, Berkeley (1995).

8. J. P. McVittie, D. S. Bang, J. S. Han, K. Hsiau, J. Li, J. Zheng and K. C. Saraswat, SPEEDIE 3.0 Manual (1995).

9. B. E. Thompson and Herbert H. Sawin, J. Appl. Phys. **63**, 2241 (1988).

10. J. Liu, G. L. Huppert and H. H. Sawin, J. Appl. Phys. **68**, 3916 (1990).

11. Robert J. Hoekstra, Michael J. Grapperhaus and Mark J. Kushner. J. Vac. Sci. Technol. A **15**, 1913 (1997).

12. A. Manenschijn and W. J. Goedheer, J. Appl. Phys. **69**, 2923 (1991).

13. Richard A. Gottscho, J. Vac. Sci. Technol. B **11**, 1884 (1993).

14. N. Sadeghi, T. Nakano, D. J. Trevor and R. A. Gottscho, J. Appl. Phys. **70**, 2552 (1991).

15. N. Sadeghi, T. Nakano, D. J. Trevor and R. A. Gottscho, J. Appl. Phys. **71**, 3648 (1992).

16. R. C. Woods, R. L. McClain, L. J. Mahoney, E. A. Den Hartog, H. Persing and J. S. Hamers, Proc. SPIE **1594**, 366 (1991).

17. T. Tokonami and T. Makabe, J. Appl. Phys. **72**, 3323 (1992).

18. B. Abraham-Shrauner and C. D. Wang, J. Appl. Phys. **77**, 3445 (1995).

19. Y. Okamoto and H. Tamagawa, J. Phys. Soc. Japan **29,** 187 (1970).

20. Wenjing Chen and Barbara Abraham-Shrauner, J. Appl. Phys. **81**, 2547 (1996).

21. S. G. Ingram and N. St J. Braithwaite, J. Phys. D **21**, 1496 (1988).

22. C. Charles, R. W. Boswell, and R. K. Porteous, J. Vac. Sci. Technol. **A 10**, 398 (1992).

23. C. Charles, J. Vac. Sci. Technol **A 11**, 157 (1993).

24. Kevin L. Junck and Getty Ward D, J. Vac. Sci. Technol. A **12,** 760 (1994).

25. J. Kim and H. Chang, Phys. Plasmas **3**, 1462 (1996).

26. J. R. Woodworth, M. E. Riley, D. C. Meister and B. P. Aragon, J. Appl. Phys. **80**, 1304 (1996).

27. J. R. Woodworth, M. E. Riley, P.A. Miller and G. A. Hebner, J. Appl. Phys. **81**, 5950 (1997).

28. J. R. Woodworth, M. E. Riley, P.A. Miller, C. A. Nichols and T. W. Hamilton, J. Vac. Sci. Technol. A **15**, 3015 (1997).

29. B. Abraham-Shrauner, J. Vac. Sci. Technol. B **12**, 2374 (1994).

30. V. K. Singh, E. S. G. Shaqfeh and J. P. McVittie, J. Vac. Sci. Technol. B **10**, 1091(1992).

31. Michael A. Lieberman and Allan J. Lichtenberg, *Principles of plasma discharges and materials processing*, (John Wiley & Sons, Inc., New York, 1994).

32. Barbara Abraham-Shrauner and W. C. Feldman, J. Geophys. Res. **77**, 618 (1976).

33. E. S. G. Shaqfeh and C. W. Jurgensen, J. Appl. Phys. **66**, 4664 (1989).

34. C. D. Wang, Private Communication (1997).

Table Captions

TABLE 1. Parameters from ICP IEDFs Simulation.

TABLE 2. Actual Parameters Calculated from the ICP with the Ar Simulation.

TABLE 3. Actual Parameters Calculated from the ICP with the Cl_2 Simulation.

Figure Captions

Figure 1. Simulated curves and measured (dots) Ar IEDFs for the ICP reactor (Ar Pressure is 10 mTorr). Measured data are plot as boxes, triangles, stars and diamonds, which correspond to the simulated curve a, b, c and d respectively.

Figure 2. Simulated curves and measured (dots) Cl_2 IEDFs for the ICP reactor (Cl_2 Pressure is 30 mTorr). Measured data are plot as boxes, triangles, stars and diamonds, which correspond to the simulated curve a, b, c and d respectively.

Figure 3. Schematic of a long trench.

Figure 4. Etch profiles for the simulated Ar IEDFs in Fig. 1.

Dimensionless time $\bar{t}$ = 1, 2, 3. Profiles correspond to Ar IEDFs.

Figure 5. Etch Profiles for the simulated Cl_2 IEDFs in Fig. 2.

Dimensionless time $\bar{t}$ = 1, 2, 3. Profiles correspond to Cl_2 IEDFs.

Figure 6. Etch Profiles for the ICP with the Cl_2 plasma if the photoresist does not etch.

Dimensionless time $\bar{t}$ = 1, 2, 3. Profiles correspond to Cl_2 IEDFs.

	# f_1	1	2
Ar	$N_s/(8.89 \times 10^{-12})(C^2m^{-2}(kg)^{-0.5})$	0.005350	0.001636820
	E'(eV)	19.7	17.8
	$T_{\|}$(eV)	0.021	0.0198
	$T_{\perp}$(eV)	0.67	0.65
Cl_2	$N_s/ (1.14\times10^{-9})(C^2m^{-2}(kg)^{-0.5})$	0.006372	0.001453
	E'(eV)	9.66	10.33
	$T_{\|}(eV^{-1})$	0.016	0.0098
	$T_{\perp}(eV^{-1})$	1.95	0.17

Table 1

	First term	Second term	Total
n (number/m^3)	5.895×10^{16}	1.803×10^{16}	7.698×10^{16}
u (m/s)	9713.7	9228.6	9600.1
$T_{\parallel}$ (eV)	0.021	0.0198	0.0207
$T_{\perp}$ (eV)	0.67	0.65	0.66
t (s)			15.4
lateral etch rate (nm/min)			84
vertical etch rate (nm/min)			1942

Table 2

	First term	Second term	Total
n (number/m^3)	5.89×10^{16}	1.34×10^{16}	7.23×10^{16}
u (m/s)	7222.4	7468.6	7268.1
$T_{\parallel}$ (eV)	0.016	0.0098	0.015
$T_{\perp}$ (eV)	1.95	0.17	1.62
t (s)			42.5
lateral etch rate (nm/min)			61.6
vertical etch rate (nm/min)			547.8

Table 3

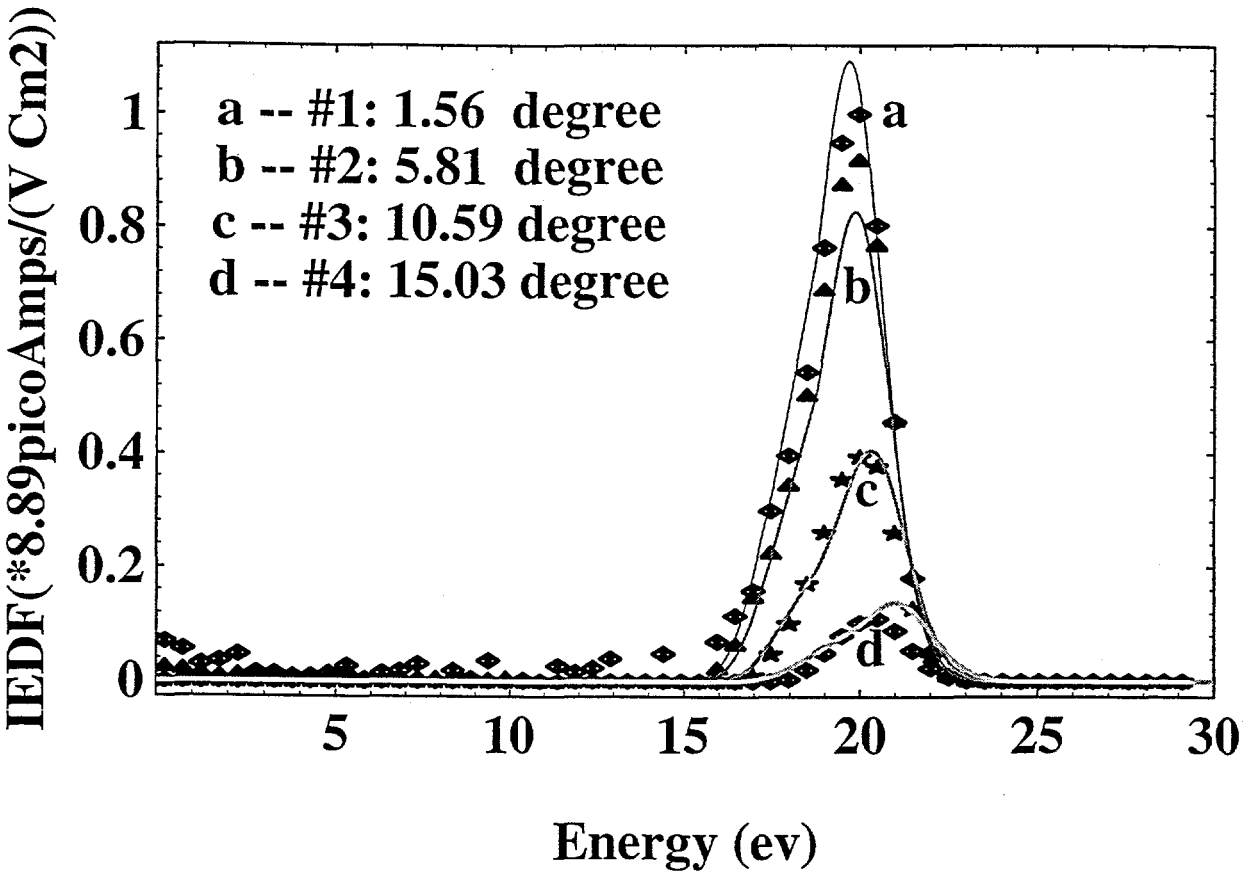
a -- #1: 1.56 degree
b -- #2: 5.81 degree
c -- #3: 10.59 degree
d -- #4: 15.03 degree
a
b
c
d
IEDF(*8.89picoAmps/(V Cm2))
Energy (ev)
0
0.2
0.4
0.6
0.8
1
5
10
15
20
25
30

Figure 1

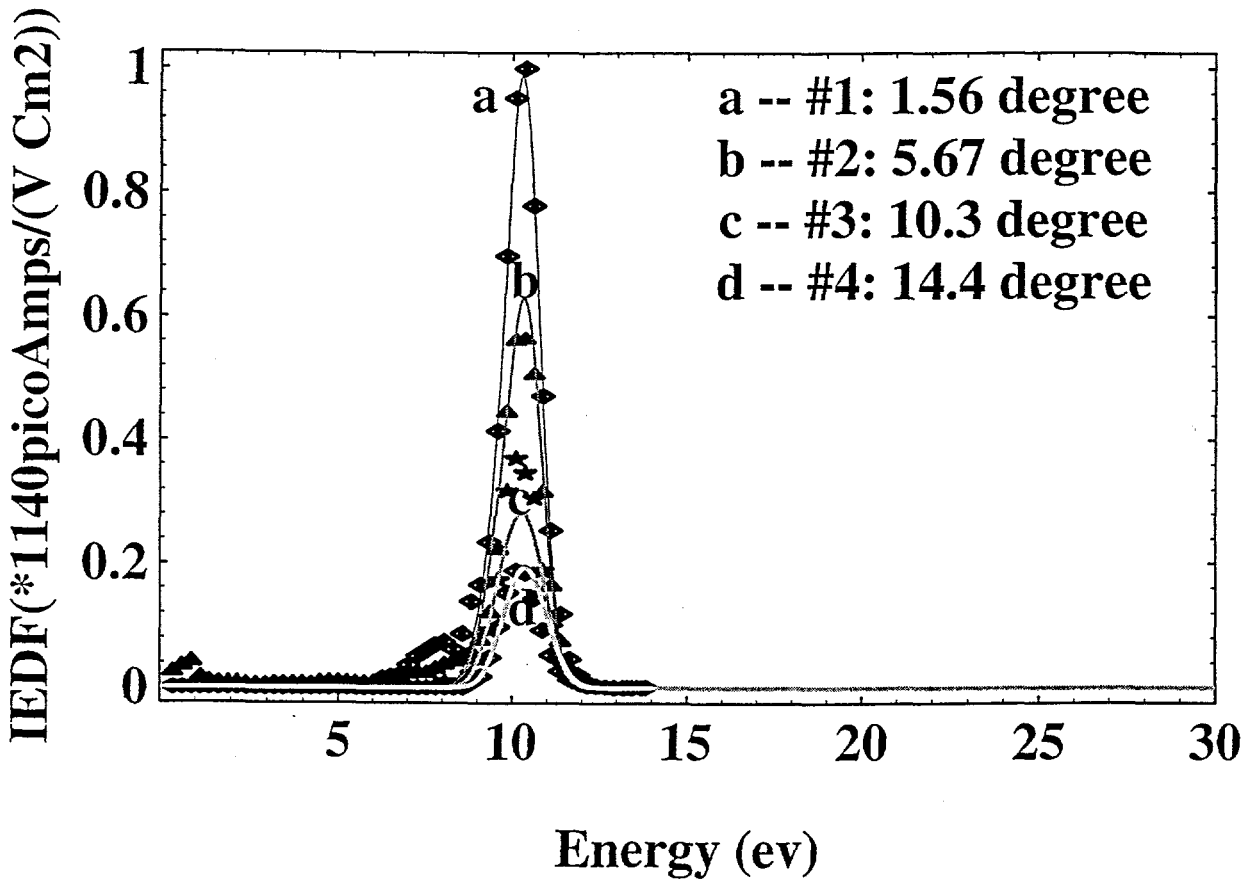
IEDF(*1140picoAmps/(V Cm2))
1
0.8
0.6
0.4
0.2
0
5
10
15
20
25
30
Energy (ev)
a
b
c
d
a -- #1: 1.56 degree
b -- #2: 5.67 degree
c -- #3: 10.3 degree
d -- #4: 14.4 degree

Figure 2

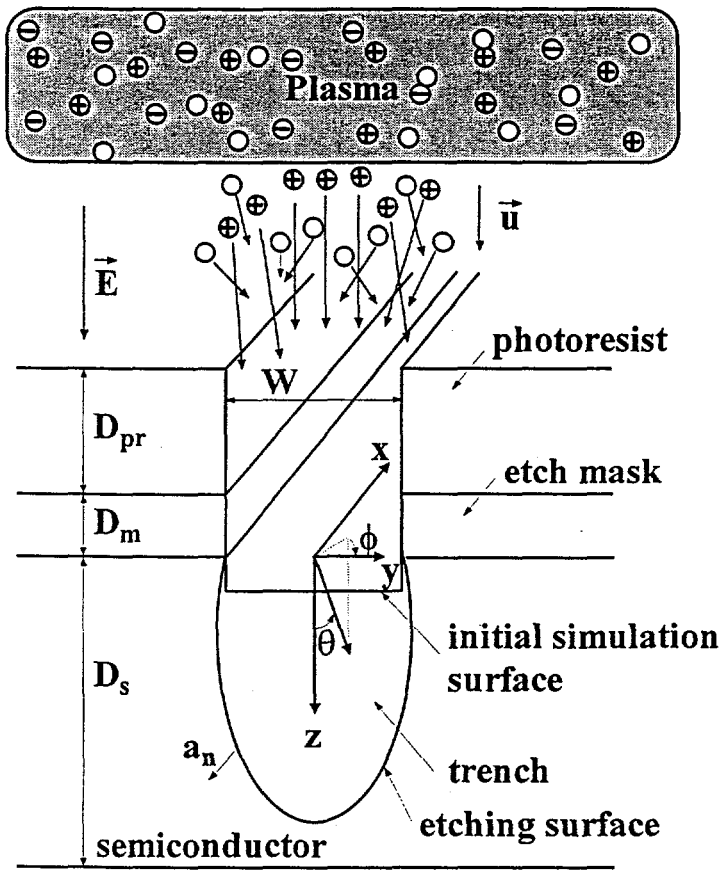
Plasma
$\vec{u}$
$\vec{E}$
photoresist
W
D_{pr}
x
etch mask
D_m
ϕ
y
initial simulation surface
θ
D_s
z
a_n
trench
etching surface
semiconductor

Figure 3

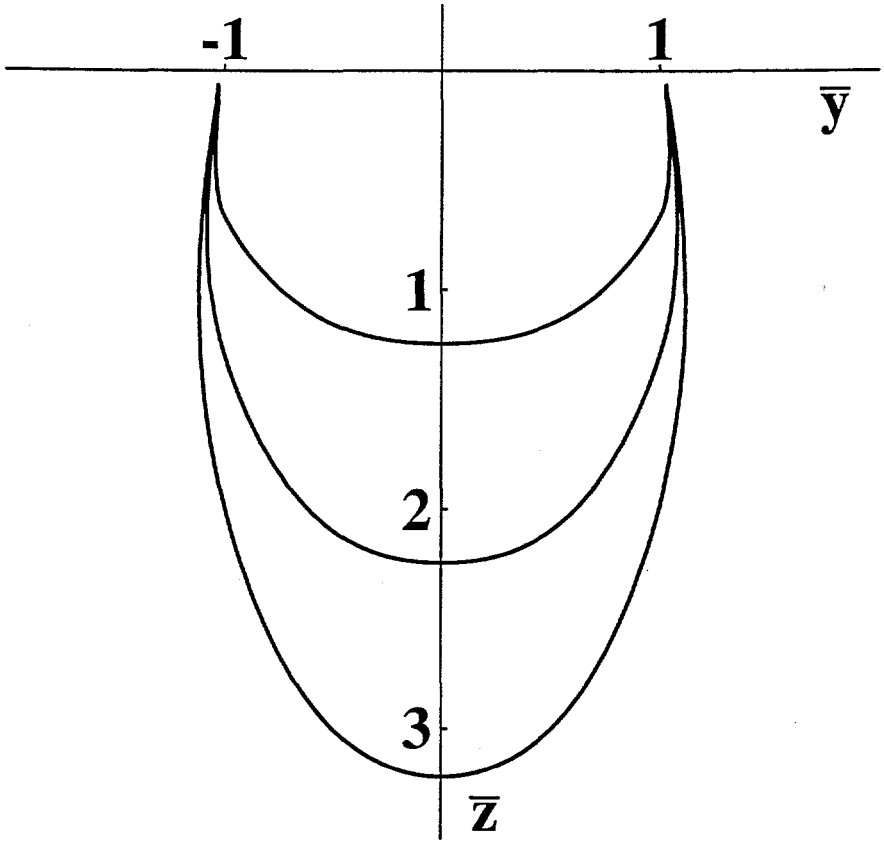

Figure 4

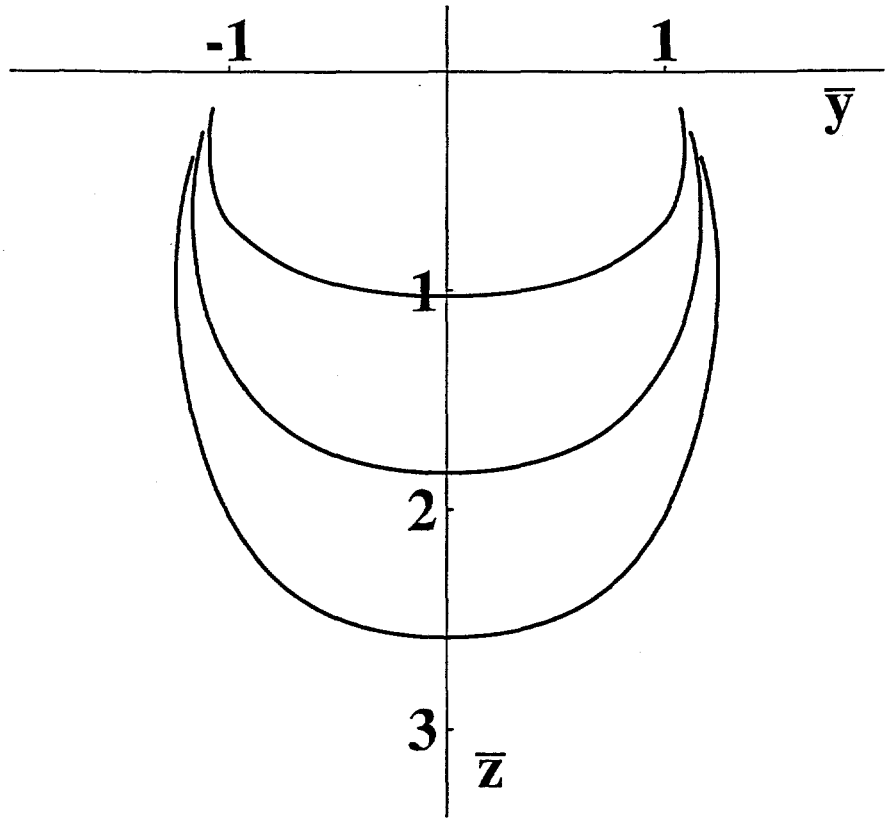

Figure 5

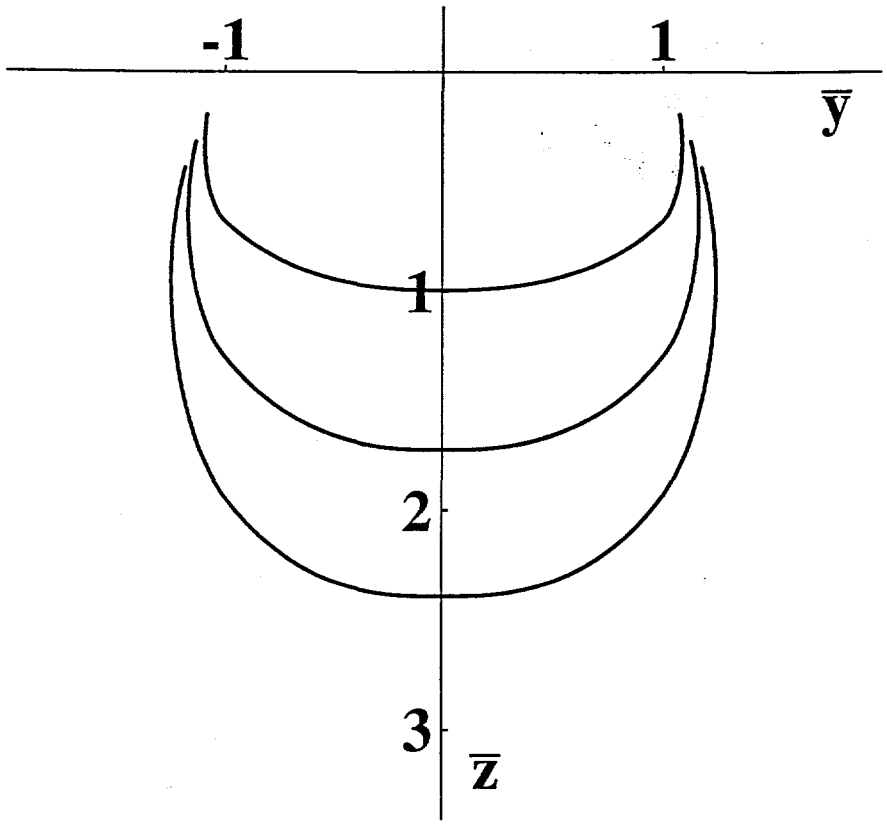

Figure 6